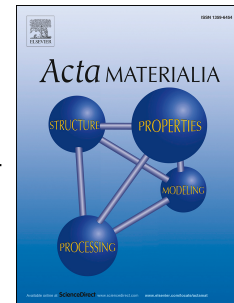


Accepted Manuscript

Topology optimization of photonic crystals with exotic properties resulting from Dirac-like cones

Yafeng Chen, Fei Meng, Guangyao Li, Xiaodong Huang



PII: S1359-6454(18)30868-1

DOI: <https://doi.org/10.1016/j.actamat.2018.10.058>

Reference: AM 14936

To appear in: *Acta Materialia*

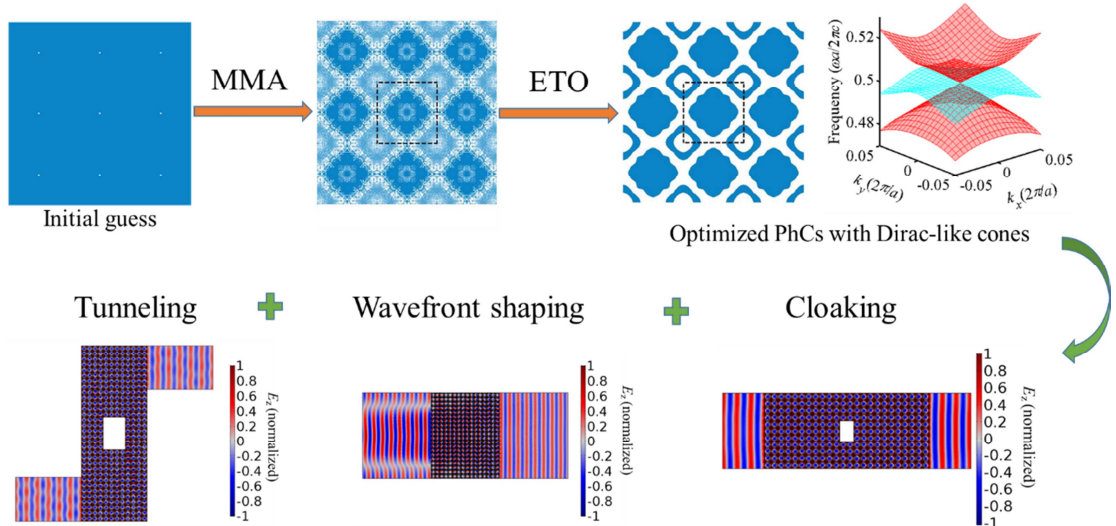
Received Date: 23 July 2018

Revised Date: 28 October 2018

Accepted Date: 29 October 2018

Please cite this article as: Y. Chen, F. Meng, G. Li, X. Huang, Topology optimization of photonic crystals with exotic properties resulting from Dirac-like cones, *Acta Materialia*, <https://doi.org/10.1016/j.actamat.2018.10.058>.

This is a PDF file of an unedited manuscript that has been accepted for publication. As a service to our customers we are providing this early version of the manuscript. The manuscript will undergo copyediting, typesetting, and review of the resulting proof before it is published in its final form. Please note that during the production process errors may be discovered which could affect the content, and all legal disclaimers that apply to the journal pertain.



Topology optimization of photonic crystals with exotic properties resulting from Dirac-like cones

Yafeng Chen^{1,2}, Fei Meng², Guangyao Li¹, Xiaodong Huang^{2,1,*}

¹*Key Laboratory of Advanced Technology for Vehicle Body Design & Manufacture, Hunan University, Changsha, 410082, China*

²*Faculty of Science, Engineering and Technology, Swinburne University of Technology, Hawthorn, VIC 3122, Australia*

Abstract

The Dirac-like cones underlie many unique properties of photonic crystals (PhCs). This paper aims to design fabrication-friendly PhCs with Dirac-like cones for transverse magnetic (TM) modes and transverse electric (TE) modes at different specific frequencies. By maximizing the minimum of a collection of the local density of states corresponding to different judiciously selected sources, this paper demonstrates that Dirac-like cones formed by the degeneracy of a doubly degenerate mode and a single mode at different desired frequencies are successfully obtained. The exotic wave manipulation properties associated with Dirac-like cones, such as cloaking, wavefront shaping and tunneling through bent channels, are exhibited based on the optimized structures. This paper also demonstrates that the proposed method could be used for the design of PhCs, with one Dirac-like cone at ω , and one monopolar band at 2ω at the Γ point and PhCs with third order Dirac-like cones, which have potential application in nonlinear optics. All topological patterns of the optimized PhCs are reported and have regular and smooth features, meaning they can be readily fabricated.

Keywords: Photonic crystals; Dirac-like cone; Third order Dirac cone; Topology optimization

1. Introduction

Dirac cones in photonic crystals (PhCs) have attracted considerable attention due to their connections to novel optical properties, such as *Zitterbewegung* of photons [1], effective zero-index behavior [2-5], topologically protected states [6, 7] and exceptional points [8, 9]. The Dirac cones in PhCs can be classified as deterministic Dirac cones and Dirac-like cones [10]. The deterministic Dirac cones, as a consequence of the lattice symmetry, have been found at the corners of the Brillouin zones for PhCs, with a triangular or honeycomb lattice. The Dirac-like cones are formed at the center of the Brillouin zone as a result of the accidental degeneracy of a doubly degenerate mode and a single mode. It has been demonstrated that Dirac-like cones in band structure have remarkable wave transport properties. For example, near the Dirac frequency, PhCs behave similarly to a zero refractive index medium [2, 3]. Simultaneously, the Dirac-like cones have potential application in nonlinear optics [8, 9, 11-13].

Designing Dirac-like cones usually requires to degenerate the resonant modes of monopolar

* Corresponding author: X. Huang, Tel: +61-3-92175633 , Fax: +61-3-92148264
E-mail: xhuang@swin.edu.au

(M) and dipolar (D) or quadrupolar (Q) profiles [10], which depends on the topology of PhCs. The traditional trial and error approach of designing Dirac-like cones in PhCs follows simple geometries based on circular pillars or air holes within a periodic lattice [2, 3, 14]. Such a design process would be inefficient and time-consuming. Even if successfully designed, the location of Dirac-like cones cannot be controlled at the desired frequency. Because the occurrence and location of Dirac-like cones in the band structure are determined by the topology of PhCs, the systematic way to design a Dirac-like cone at a desirable frequency should be by formulating the problem with appropriate objective functions and constraints, and then solving it using topology optimization. Topology optimization originally proposed in elastic fields seeks the most appropriate materials layout within a given design domain so that the resulting structures have the best performance, such as minimum compliance [15-19]. In the last decade, topology optimization has been employed to design novel PhCs and devices with exotic and desirable properties [20-32].

Sigmund and Jensen [31] proposed two-stage optimization to design PhCs with an optimal partial band gap (PBG). Meng et al. [26-28] maximized PBG and a complete band gap for both symmetric and asymmetric PhCs using the bi-directional evolutionary structural optimization (BESO) method. Wang et al. [32] presented topology optimization of slow light in PhCs using a robust design formulation while Jensen et al. [30] reduced the loss in PhCs waveguide by topology optimization. Zhou et al. [33] conducted topology optimization for negative permeability metamaterials using the level-set algorithm and Lin et al. [25] achieved high-efficiency second harmonic generation in wavelength-scale photonic structures based on topology optimization. Piggott et al. [22] demonstrated inverse design for high-efficiency, small-footprint couplers between arbitrary nanophotonic waveguide modes in two dimensions. Recent developments in topology optimization of photonic structural materials and phononic crystals had been reviewed in Jensen and Sigmund [20], Yi and Youn [34] and Molesky et. al. [35].

Despite this, the topological design of PhCs for Dirac-like cones remains lacking. Liang and Johnson [21] investigated the topology optimization of optical micro-cavities based on the frequency-averaged local density of states (LDOS). This research demonstrated that the concept of LDOS provides an effective and efficient method for achieving a single resonant mode of PhCs. Recently, Lin et al. [9, 36] extended the optimization formulation for a single resonant mode to a multi-mode degeneracy. By maximizing the minimum of the collection of LDOSs corresponding to different sources at the given frequency, the PhCs with third-order Dirac-like cones [9] and dual-polarization Dirac-like cones [36] were successfully achieved. However, they uncovered increased functionalities for Dirac-like cones in PhCs. Thus, the operation frequencies are elaborately selected for dielectric materials with different refractive indexes, and the optimized topology contains a large portion of intermediate elements as a result of fine-tuning the necessary modal frequencies. Although the intermediate elements are partly avoided by imposing the filter and penalization schemes, some of the optimized structures have many tiny features or exhibit 'barcode' characteristics, which causes difficulties in manufacturing. Because multiple topological designs of PhCs may achieve Dirac-like cones and therefore the solution highly depends on the optimization parameters and algorithm used. Regarding the application of Dirac-like cones, this paper aims to design fabrication-friendly PhCs with Dirac-like cones for transverse magnetic (TM) modes and transverse electric (TE) modes at different specified frequencies.

The optimization problem has been formulated to maximize the minimum of a collection of LDOSs corresponding to different judiciously selected sources. This paper proposes a two-

stage optimization procedure to ensure the optimized topologies possess fabrication-friendly characteristics. Numerical examples demonstrate that all optimized topologies have clear and smooth boundaries, which can be easily fabricated. The exotic properties associated with Dirac-like cones, such as cloaking, wavefront shaping and tunneling through bent channels, are demonstrated based on the optimized PhCs. The remaining sections of this paper are organized as follows. Section 2 introduces the concept of LDOS formation and finite element analysis to solve the LDOS. In Section 3, the mathematical formulation of the optimization problem and elemental sensitivities are derived and numerical examples optimized directly by the method of moving asymptotes (MMA) [19, 37] are presented. The evolutionary topology optimization algorithm (ETO) is introduced in Section 4 and several numerical examples of Dirac-like cones for TM modes and TE modes are presented at different specific frequencies. Section 5 exhibits exotic wave manipulation properties associated with Dirac-like cones based on the optimized PhCs. In Section 6, topology optimization for extended Dirac-like problems is conducted. The conclusions are drawn in Section 7.

2 Formulation of local density of states and finite element analysis

2.1 Formulation of local density of states

Previous studies indicate that the concept of LDOS provides an elegant method for deliberately triggering the desired resonant mode of a structure [9, 21, 36]. The LDOS is proportional to the power radiated by a time harmonic current source, $\mathbf{J}(\mathbf{r}, \omega) = \mathbf{J}(\mathbf{r})e^{-i\omega t}$ and can be expressed by

$$LDOS(\omega, \mathbf{J}(\mathbf{r})) = -\frac{6}{\pi} \operatorname{Re} \left[\int \mathbf{J}^*(\mathbf{r}) \cdot \mathbf{E}(\mathbf{r}) d\mathbf{r} \right] \quad (1)$$

in which $\mathbf{J}^*(\mathbf{r})$ denotes the complex conjugate of $\mathbf{J}(\mathbf{r})$, and $\mathbf{J}(\mathbf{r}) = \delta(\mathbf{r} - \mathbf{r}_0) \hat{\mathbf{e}}_j$ is the incident current in direction (unit vector) $\hat{\mathbf{e}}_j$ at position \mathbf{r}_0 . $\mathbf{E}(\mathbf{r})$ is the solution of the local Maxwell's equation under the incident current, $\mathbf{J}(\mathbf{r}, \omega)$, as [38],

$$\nabla \times \frac{1}{\mu(\mathbf{r})} \nabla \times \mathbf{E}(\mathbf{r}) - \epsilon(\mathbf{r}) \omega^2 \mathbf{E}(\mathbf{r}) = i\omega \mathbf{J}(\mathbf{r}) \quad (2)$$

in which $\epsilon(\mathbf{r})$ and $\mu(\mathbf{r})$ are the permittivity and permeability of a dielectric material. However, eqn. (2) cannot be solved for an infinite periodic medium such as PhCs. To circumvent this difficulty, the frequency-average LDOS [9, 21, 36] of the primitive unit cell, instead of the LDOS at a single discrete frequency, can be easily calculated in the vicinity of ω as

$$L(\omega, \mathbf{J}(\mathbf{r})) = \int_{-\infty}^{\infty} LDOS(\tilde{\omega}, \mathbf{J}(\mathbf{r})) W(\omega, \tilde{\omega}) d\tilde{\omega} \quad (3)$$

in which $W(\omega, \tilde{\omega})$ is the weight function and $\tilde{\omega}$ is the variable of integration. Here, the simple Lorentzian weight function over the upper-half bandwidth Γ between ω and $\omega + i\Gamma$ was chosen as,

$$W(\omega, \tilde{\omega}) = \frac{\Gamma/\pi}{(\tilde{\omega} - \omega)^2 + \Gamma^2} \quad (4)$$

Using the contour integration techniques [21], the frequency-averaged LDOS becomes

$$L(\omega, \mathbf{J}(\mathbf{r})) = LDOS(\omega + i\Gamma, \mathbf{J}(\mathbf{r})) \quad (5)$$

Thus, the scattering problem Eq. (2) at a complex frequency, $\omega + i\Gamma$, can be written as,

$$\nabla \times \frac{1}{\mu(\mathbf{r})} \nabla \times \mathbf{E}(\mathbf{r}) - \epsilon(\mathbf{r})(\omega + i\Gamma)^2 \mathbf{E}(\mathbf{r}) = i(\omega + i\Gamma) \mathbf{J}(\mathbf{r}) \quad (6)$$

and then,

$$\nabla \times \frac{1}{\mu(\mathbf{r}) \left(1 + i \frac{\Gamma}{\omega}\right)} \nabla \times \mathbf{E}(\mathbf{r}) - \epsilon(\mathbf{r}) \left(1 + i \frac{\Gamma}{\omega}\right) \omega^2 \mathbf{E}(\mathbf{r}) = i\omega \mathbf{J}(\mathbf{r}) \quad (7)$$

The above equation is equivalent to a scattering problem at the real frequency ω with lossy materials $\tilde{\epsilon}(\mathbf{r}) = \epsilon(\mathbf{r}) \left(1 + i \frac{\Gamma}{\omega}\right)$ and $\tilde{\mu}(\mathbf{r}) = \mu(\mathbf{r}) \left(1 + i \frac{\Gamma}{\omega}\right)$. In the following optimization, we will gradually decrease the loss of material, Γ , until the desired solution is stably achieved [21].

The above frequency-averaged LDOS can be used to any extended Bloch mode in a periodic medium for an arbitrary wave vector \mathbf{k} by applying the corresponding periodic boundary condition for the primitive unit cell. Because the focus is on the Bloch modes at the Γ point in which $\mathbf{k} = (0,0)$, the periodic boundary condition of the primitive unit cell is equivalent to the continuum boundary condition.

2.2 Finite element analysis

To compute the frequency-averaged LDOS, the primitive unit cell is discretized with finite elements. Thus, the $\mathbf{E}(\mathbf{r})$ and $\mathbf{J}(\mathbf{r})$ are respectively expressed by,

$$\mathbf{E}(\mathbf{r}) = \sum_e \sum_{i=1}^m N_i(\mathbf{r}) E_i^e \quad (8)$$

$$\mathbf{J}(\mathbf{r}) = \sum_e \sum_{i=1}^m N_i(\mathbf{r}) J_i^e \quad (9)$$

in which e denotes the element and m is the total number of nodes for each element. $N = \{N_1, N_2, N_3, N_4\}$ is the standard shape function for a four node quadrilateral element. Following the standard formulation of the finite element method, the scattering problem in eqn. (7) can be written as,

$$(\mathbf{K} - \omega^2 \mathbf{M}) \mathbf{E} = i\omega \mathbf{J} \quad (10)$$

in which \mathbf{E} and \mathbf{J} are the nodal vectors for the electric field and point source. \mathbf{K} and \mathbf{M} are

$$\mathbf{K} = \sum_e \frac{\mathbf{K}^e}{\tilde{\mu}_e} \quad \text{and} \quad \mathbf{M} = \sum_e \tilde{\epsilon}_e \mathbf{M}^e \quad (11)$$

in which the summation denotes the assembly of the following elemental matrices,

$$\mathbf{K}^e = \int_A \frac{\partial \mathbf{N}^T}{\partial x} \frac{\partial \mathbf{N}}{\partial x} + \frac{\partial \mathbf{N}^T}{\partial y} \frac{\partial \mathbf{N}}{\partial y} dA$$

$$\mathbf{M}^e = \int_A \mathbf{N}^T \mathbf{N} dA$$

in which A denotes the total area of an element. By solving eqn. (10), the frequency-averaged LDOS can be computed as,

$$L(\omega, \mathbf{J}) = -\frac{6}{\pi} \operatorname{Re}(\mathbf{J}^* \cdot \mathbf{E}) \quad (12)$$

3. Topology optimization formulation

3.1 Optimization problems

Topology optimization here aims to find Dirac-like cones at an arbitrary frequency, resulting from the requisite M, D and Q modes. In this paper, the PhCs are forced with C_{4v} symmetry. To trigger the desired mode, the current \mathbf{J} should be properly placed, as illustrated in Fig. 1. Topology optimization will maximize the corresponding frequency-averaged LDOS or equivalently minimize the inverse of the frequency-averaged LDOS. Here, the primitive unit cell is assumed to be constructed by two materials: material 1 with permittivity ϵ_1 and material 2 with ϵ_2 ($\epsilon_2 > \epsilon_1$). The permeabilities of the two materials are the same, $\mu_1 = \mu_2$. Thus, the frequency-averaged LDOS depends on the spatial distribution of those constituent materials, as well as the resulting solution of eqn. (7). To this end, the topology optimization problem based on the finite element model can be expressed by

$$\begin{cases} \text{Find : } x_e \ (e = 1, 2, \dots, N) \\ \min : \frac{1}{L(\omega, \mathbf{J}, \mathbf{E})} \\ \text{s.t.: } (\mathbf{K} - \omega^2 \mathbf{M}) \mathbf{E} = i\omega \mathbf{J} \\ x_e \in \{0, 1\} \end{cases} \quad (13)$$

in which x_e is discrete design variables. $x_e = 0$ means that the element is full of material 1 and $x_e = 1$ for material 2.

Fig. 1. Schematic diagram for the position of the source to obtain the desired mode: (a) \mathbf{J}_1 for M mode; (b) \mathbf{J}_2 for D mode; (c) \mathbf{J}_3 for Q mode.

To form Dirac-like cones, it must find a multi-mode degeneracy: for example, two kinds of degeneration modes triggered by currents \mathbf{J}_1 and \mathbf{J}_2 , respectively. In this case, we have to minimize the maximum one from the collection of inverse frequency-averaged LDOSs at the desired frequency ω . Such a min-max problem is usually non-differentiable. However, this non-differentiability can be overcome by recasting the problem in a so-called bound formulation [19, 20] as

$$\begin{cases} \text{Find : } x_e \ (e = 1, 2, \dots, N) \\ \min : t = \max \left\{ \frac{1}{L_1(\omega, \mathbf{J}_1, \mathbf{E}_1)}, \frac{1}{L_2(\omega, \mathbf{J}_2, \mathbf{E}_2)}, \dots \right\} \\ \text{s.t.: } (\mathbf{K} - \omega^2 \mathbf{M}) \mathbf{E}_1 = i\omega \mathbf{J}_1, (\mathbf{K} - \omega^2 \mathbf{M}) \mathbf{E}_2 = i\omega \mathbf{J}_2, \dots \\ t \geq \frac{1}{L_1(\omega, \mathbf{J}_1, \mathbf{E}_1)}, t \geq \frac{1}{L_2(\omega, \mathbf{J}_2, \mathbf{E}_2)}, \dots \\ x_e \in \{0, 1\} \end{cases} \quad (14)$$

in which L_1, L_2, \dots denote the frequency-averaged LDOSs emitted by the current $\mathbf{J}_1, \mathbf{J}_2, \dots$, respectively. t in the objective function denotes the maximum of the inverse L_1, L_2, \dots and its value acts as the upper bound of the inverse L_1, L_2, \dots in each iteration. Driven by the minimization of the objective function and the imposed constraints, the resulting values of the

inverse L_1 , L_2 , ... must be less than (or equal to in very few cases) the current value of t . t is updated step by step and its value becomes smaller and smaller, which can be confirmed by the following numerical examples. The above min-max problem is complex. The main difficulty is due to the discrete design variables. To overcome this problem, the design variable, x_e , can be relaxed to be continuous as $0 \leq x_e \leq 1$. The linear interpolation scheme is adopted for the permittivity ϵ of the material as,

$$\epsilon(x_e) = (1 - x_e)\epsilon_1 + x_e\epsilon_2 \quad (15)$$

in which subscripts 1 and 2 represent material phases 1 and 2, respectively. As such, the original topology optimization problem in eqn. (14) can be solved by the standard optimizer, such as the method of moving asymptotes (MMA) [19, 37]. Because the frequency, at which the Dirac cone will occur, and its corresponding current sources should be specified by the user, they are constants during the entire optimization process. For simplicity, the dependence of ω and \mathbf{J} shall be omitted from $L(\omega, \mathbf{J}, \mathbf{E})$ and written as $L(\mathbf{E})$, hereafter.

3.2 Sensitivity analysis

To solve the above optimization problem, the sensitivity of the frequency-averaged LDOS, $L(\mathbf{E})$ is required. According to eqn. (12), its sensitivity can be expressed by,

$$\frac{\partial L(\mathbf{E})}{\partial x_e} = -\frac{6}{\pi} \operatorname{Re} \left(\mathbf{J}^* \cdot \frac{\partial \mathbf{E}}{\partial x_e} \right) \quad (16)$$

To calculate the term $\frac{\partial \mathbf{E}}{\partial x_e}$, $L(\mathbf{E})$ can be re-written by introducing the scattering equation as,

$$L(\mathbf{E}) = -\frac{6}{\pi} \operatorname{Re} \left\{ \mathbf{J}^* \cdot \mathbf{E} + \boldsymbol{\lambda}^T \cdot [i\omega \mathbf{J} \cdot (\mathbf{K} - \omega^2 \mathbf{M}) \mathbf{E}] \right\} \quad (17)$$

in which $\boldsymbol{\lambda}$ is the Lagrangian multiplier, which can be chosen to be any value once the scattering equation is satisfied. Then,

$$\begin{aligned} \frac{\partial L(\mathbf{E})}{\partial x_e} &= -\frac{6}{\pi} \operatorname{Re} \left\{ \mathbf{J}^* \cdot \frac{\partial \mathbf{E}}{\partial x_e} - \boldsymbol{\lambda}^T \cdot \left[\frac{\partial (\mathbf{K} - \omega^2 \mathbf{M})}{\partial x_e} \mathbf{E} + (\mathbf{K} - \omega^2 \mathbf{M}) \frac{\partial \mathbf{E}}{\partial x_e} \right] \right\} \\ &= -\frac{6}{\pi} \operatorname{Re} \left\{ \boldsymbol{\lambda}^T \cdot \frac{\partial (\mathbf{K} - \omega^2 \mathbf{M})}{\partial x_e} \mathbf{E} + [\mathbf{J}^* - \boldsymbol{\lambda}^T \cdot (\mathbf{K} - \omega^2 \mathbf{M})] \frac{\partial \mathbf{E}}{\partial x_e} \right\} \end{aligned} \quad (18)$$

To eliminate $\frac{\partial \mathbf{E}}{\partial x_e}$, let

$$\mathbf{J}^* - \boldsymbol{\lambda}^T \cdot (\mathbf{K} - \omega^2 \mathbf{M}) = 0 \quad (19)$$

Comparing the above adjoint equation with eqn. (10) and using the properties that $\mathbf{K} - \omega^2 \mathbf{M}^T$ is complex symmetric [$\mathbf{K} - \omega^2 \mathbf{M} = (\mathbf{K} - \omega^2 \mathbf{M})^T$] and \mathbf{J} is real ($\mathbf{J}^* = \mathbf{J}^T$), the Lagrangian multiplier can be chosen as

$$\boldsymbol{\lambda} = \frac{\mathbf{E}}{i\omega} = -\frac{i\mathbf{E}}{\omega} \quad (20)$$

Substituting eqn. (20) into eqn. (18), the sensitivity of the frequency-averaged LDOS is rewritten as

$$\frac{\partial L(\mathbf{E})}{\partial x_e} = \frac{6}{\pi\omega} \operatorname{Re} \left(i\mathbf{E}^T \cdot \frac{\partial (\mathbf{K} - \omega^2 \mathbf{M})}{\partial x_e} \mathbf{E} \right) \quad (21)$$

Given the expressions in eqns. (11) and (15), the derivative of matrices \mathbf{K} and \mathbf{M} are

$$\frac{\partial \mathbf{K}}{\partial x_e} = 0 \quad (22a)$$

$$\frac{\partial \mathbf{M}}{\partial x_e} = (\tilde{\epsilon}_2 - \tilde{\epsilon}_1) \mathbf{M}^e \quad (22b)$$

in which $\tilde{\epsilon}_1$ and $\tilde{\epsilon}_2$ denote the complex permittivity of materials 1 and 2, as explained below eqn. (7), respectively. Substituting eqns. (22a) and (22b) into eqn. (21), the sensitivity of the frequency-averaged LDOS can be simplified as,

$$\frac{\partial L(\mathbf{E})}{\partial x_e} = \frac{6\omega(\tilde{\epsilon}_2 - \tilde{\epsilon}_1)}{\pi} \operatorname{Re}(i\mathbf{E}^T \cdot \mathbf{M}^e \mathbf{E}) \quad (23)$$

3.3 Optimization for Dirac-like cones

Based on the sensitivity given in eqn. (23), the optimization problem in eqn. (14) can be directly solved using MMA [19] at the first stage. Here, it is assumed that the unit cell of square lattice PhCs has a high symmetry, C_{4v} . The optimization objective is to minimize $\max\{1/L_1, 1/L_2\}$ or $\max\{1/L_2, 1/L_3\}$, which is equivalent to maximize $\min\{L_1, L_2\}$ or $\min\{L_2, L_3\}$, so that resonant modes of duplicated D modes and a single M or Q mode are degenerated and form Dirac cones [10]. The dielectric constants of two constituent materials are $\epsilon_1=1$, e.g., air, and $\epsilon_2=5.5$, e.g., silicon nitride. In the following figures, material 1 and material 2 in the primitive unit cell are represented by white and light blue, respectively. For simplicity, all frequencies are normalized by $\Omega = \omega a / 2\pi c$, in which c is the speed of light in air.

Using an example for a Dirac point of TM mode at the target frequency, $\Omega = 0.5$, Figure 2 demonstrates the iteration history of the objective function, $\min(L_1, L_2)$, which stably increases from nearly zero to its maximum. Simultaneously, the Dirac error, $\tau = \sqrt{(\Omega_M - \Omega)^2 + 2(\Omega_D - \Omega)^2}$, is defined to measure the quality of the resulting Dirac point, in which Ω_M and Ω_D are the frequencies of the monopole and dipole bands, respectively. As demonstrated in Fig. 2, the Dirac error gradually decreases from its initial value that is larger than zero and finally converges to a nearly zero value. This indicates that the expected Dirac point has successfully been obtained.

Fig. 2. Iteration history of $\min(L_1, L_2)$, Dirac error and topology of the primitive unit cell.

Figures 3 and 4 provide optimized topologies of the unit cells, the obtained Dirac points at the band structure and Dirac-like cones for TM modes and TE modes at various frequencies. As can be observed in the band structures, two double D bands and one M or Q band (red lines) are accidentally degenerated to one point at the specified frequencies. These bands form the Dirac-like cones (red surfaces in Figs. 3(c) and (f), Figs. 4(c) and (f)) intersecting a quadratic dispersion band (green surfaces) at the Dirac-like point. Although the expected Dirac-like cones are successfully obtained, the optimized topologies are complex and difficult to manufacture. The difficulties arise from the following facts. The optimized design contains many intermediate elements whose dielectric constant is between ϵ_1 and ϵ_2 . Our numerical

experience showed that the penalty scheme [16] relieves the occurrence of intermediate elements to a certain extent, but are still unavoidable. Secondly, the optimized topologies contain many tinny features, which cause the manufacturing difficulty. The material distribution of the optimized topologies is based on piece-wise elements, which may cause zig-zag boundaries. To ensure the optimized design with fabrication-friendly features, this paper proposes an ETO algorithm in the next section. The obtained topologies in this section will be used as the initial topologies of ETO.

Fig. 3. Optimized PhCs and their band diagrams for TM modes: (a,d) optimized 3×3 primitive unit cells (light blue-dielectric material, white-air, hereinafter the same) for $\omega a/2\pi c = 0.5$ and 0.6 , respectively; (b,e) corresponding band structures, the inserts denote that the Dirac-like cones are formed by the degeneracy of two D modes and one M mode; (c,f) zooms in of three-dimensional dispersion surfaces near the Dirac-like cones (denoted as dash box in the band structure). k_x and k_y denote the Bloch wave vector along the direction x and y , respectively.

Fig. 4. Optimized PhCs and their band diagrams for TE modes: (a,d) optimized 3×3 primitive unit cells (light blue - dielectric material, white - air, hereinafter the same) for $\omega a/2\pi c = 0.6$ and 0.7 , respectively; (b,e) corresponding band structures, the inserts denote that the Dirac-like cone is formed by the degeneracy of two D modes and one single mode (M or Q); (c,f) close-up of three-dimensional dispersion surfaces close to the Dirac-like cones (denoted as a dashed box in the band structure).

4. Evolutionary topology optimization

4.1 Evolutionary topology optimization algorithm

To achieve optimized PhCs with fabrication-friendly features, an evolutionary topology optimization (ETO) algorithm is developed here. ETO will evolve the distribution of constituent materials from an optimized design resulting from MMA at the first stage. It should be noted that the ideal boundary between two constituent materials should be smooth, as denoted in Fig. 5; the smooth boundary divides the design variables into three categories as

$$\begin{cases} x_e = 0 & x_e \in \Omega_1 \\ 0 < x_e < 1 & x_e \text{ on } \Gamma \\ x_e = 1 & x_e \in \Omega_2 \end{cases} \quad (24)$$

in which Ω_1 and Ω_2 mean the domains of materials 1 and 2, respectively. Γ is the smooth boundary between materials 1 and 2. It should be noted that a boundary intermediate element means that the element is partly covered by material 1 or material 2, which is physically different from the piece-wise intermediate element in MMA. Thus, x_e can be considered as the volume fraction of material 2, which can be figured out by the boundary geometry within the element. The boundary geometry will be changed during optimization, which complicates the calculation of x_e . Fine grid points, x_j , were artificially assigned within each element and, as such, x_e can be approximately expressed by

$$x_e = \frac{\sum_{j=1}^{N_e} x_j}{N_e} \quad (25)$$

in which N_e is the total number of grip point within element e , and $x_j \in \{0,1\}$. The permittivity at a grid point is expressed by

$$\epsilon(x_j) = (1 - x_j)\epsilon_1 + x_j\epsilon_2 = \begin{cases} \epsilon_1 & \text{for } x_j = 0 \\ \epsilon_2 & \text{for } x_j = 1 \end{cases} \quad (26)$$

Fig. 5 clearly illustrates the relationships among mesh, boundary, grid point and elemental volume fraction. Meanwhile, the linear material interpolation for the volume fraction of an element, x_e is used, which is the same as eqn. (15) for the density of an element.

Fig. 5. Mesh, smooth boundary, density of grid points x_j , and volume fraction of an element x_e are used in ETO.

With the above settings, ETO will regularize the optimized solution, x_e , resulting from the first stage optimization and calculate x_j . The filtering scheme can be used for directly converting the values of x_e to grip points and eliminating the tinny feature of geometry. However, such a process requires an expensive computational cost. In doing so, x_e is first filtered to elemental nodes as

$$x^n = \frac{\sum w_e x_e}{\sum w_e} \quad (27)$$

in which x^n denotes the variable of the n th node. w_e is a linear weight factor as

$$w_e = \max[0, r_{\min} - r(e, n)] \quad (28)$$

in which $r(e, n)$ denotes the distance between the n th node and the center of element e . r_{\min} is the filter radius specified by the user, which is set to be one element length in this paper.

Next, the variables of elemental nodes are linearly interpolated to grid points by using shape function. Here, taking a four node element as an example, the variable at any point $x_j(\xi, \eta)$ within an element can be expressed by

$$x_j(\xi, \eta) = \sum_{k=1}^4 N^k(\xi, \eta) x_e^k \quad (29)$$

in which (ξ, η) is the local coordinator of the point and x_e^k is the variable at the k th node of element e . The shape functions

$$N^k(\xi, \eta) = \frac{1}{4} (1 + \xi^k \xi)(1 + \eta^k \eta) \quad (30)$$

in which (ξ^k, η^k) ($k=1,2,3,4$) is the local coordinator for the k th node of the element. Thus, the variable at all grid points can be calculated accordingly.

To obtain a solid/void design at grid points, the variable of grid points is expressed by the Heaviside step function as

$$x_j = \begin{cases} 1 & \text{if } x_j > th \\ 0 & \text{if } x_j < th \end{cases} \quad (31)$$

in which the threshold value, th , can be easily determined by ensuring the volume fraction of material 2 to be equal to the one before filtering. Then, x_e is updated according to eqn. (25) for the next round finite element analysis.

4.2 Manufacturing-friendly designs

This section will present several numerical examples resulting from ETO. As an example, Fig. 6 demonstrates the iteration histories of $\min(L_1, L_2)$, Dirac error and topology of the primitive unit cell. It can be observed that the initial design after the ETO regularization has a large Dirac error, which will be decreased step by step. Finally, the Dirac error stably converges to a value of nearly zero, which means the expected Dirac point is achieved. Most importantly, the optimized topology becomes clearer and the final design possesses smooth boundaries.

Fig. 6. Iteration history of $\min(L_1, L_2)$, Dirac error and topology of the primitive unit cell resulting from ETO.

Figure 7 presents three optimized PhCs with 3×3 unit cells (the primitive unit cell is given in the dashed box) by ETO and their band structures for TM modes at different frequencies. The desired frequencies are $\omega a/2\pi c = 0.5, 0.55$ and 0.6 , respectively. As can be observed in the band structures, two doubly degenerated D bands and one M band (red lines) are accidentally degenerated at the desired frequency. As the three-dimensional dispersion surfaces near the Dirac-like cones demonstrate, these bands form the Dirac-like cone (red) intersecting a quadratic dispersion band (green) at the Dirac-like point. Figure 8 presents three numerical examples of TE modes for the desirable frequencies, being $\omega a/2\pi c = 0.6, 0.65$ and 0.7 , respectively. The Dirac-like cone for $\omega a/2\pi c = 0.6$ is degenerated by two D modes and one M mode, while they are degenerated by two D modes and one Q mode for $\omega a/2\pi c = 0.65$ and 0.7 . All the topological patterns of the optimized PhCs have smooth boundaries, meaning that they can be readily fabricated.

Fig. 7. Optimized PhCs for Dirac-like cones of TM modes at different frequencies by ETO, their band structures and close-ups in of three-dimensional dispersion surfaces near the Dirac-like cones: (a) $\omega a/2\pi c = 0.50$; (b) $\omega a/2\pi c = 0.55$; (c) $\omega a/2\pi c = 0.60$.

Fig. 8. Optimized PhCs for Dirac-like cones of TE modes at different frequencies by ETO, their band structures and close-ups of three-dimensional dispersion surfaces near the Dirac-like cones: (a) $\omega a/2\pi c = 0.60$; (b) $\omega a/2\pi c = 0.65$; (c) $\omega a/2\pi c = 0.70$.

5. Zero index associated with Dirac-like cones

One of the exotic properties associated with the Dirac-like cone is the zero index behavior,

which can realize the special manipulation of light waves, such as cloaking, wavefront shaping and tunneling [2, 3]. This research will take the optimized PhCs for TM modes at $\omega a/2\pi c = 0.5$ (PhC-TM05) and TE modes at $\omega a/2\pi c = 0.6$ (PhC-TE06) as examples. The commercial finite element analysis software, COMSOL Multiphysics, is used for simulation. The boundary conditions are perfect magnetic conductors for PhC-TM05 and perfect electric conductors for PhC-TE06.

First, the effective optical properties of PhC-TM05 and PhC-TE06 are calculated using the S-parameter retrieval [39] by using the full wave analysis within the frequency domain. The results in Fig. 9 indicate that simultaneous zero effective permittivity (ϵ_{eff}) and permeability (μ_{eff}) are successfully obtained at the corresponding Dirac frequencies.

Fig. 9. Effective permittivity (ϵ_{eff}) and permeability (μ_{eff}) for PhC-TM05 and PhC-TE06

Next, a PhC array is constructed consisting of 24×11 unit cells with 2×3 unit cells at the center removed, acting as the obstacle. Figures 10(a) and (c) demonstrate that light wave at the Dirac frequency simply passes through the PhCs by preserving their plane wave character as if the obstacle is not there. By contrast, Figures 10(b) and (d) demonstrate that if the PhCs are removed, the plane wavefront is destroyed by the obstacle. Comparing Figs. 10(a) and (c) with Figs. 10(b) and (d) demonstrates that the optimized PhCs at the Dirac frequency can guide a wave around an obstacle inside a channel, clearly exhibiting the cloaking effect.

Fig. 10. Full wave simulation illustrating the cloaking effect: (a) normalized electric field distribution (E_z) for PhC-TM05; (b) control simulation with the PhC-TM05 removed; (c) normalized magnetic field distribution (H_z) for PhC-TE06; (d) control simulation with the PhC-TE06 removed.

Another PhCs array consisting of 16×20 unit cells is constructed and impinged by a Gaussian beam at a frequency slightly higher than the Dirac frequency, which is selected to avoid exciting the flat band [2]. As shown in Figs. 11(a) and (c), the output waves are shaped with plane wave wavefront. Figures 11(b) and (d) show that when the PhCs are removed, such a wavefront shaping effect disappears. Figure 12 demonstrates that waves at the Dirac frequency can turn through a bent waveguide, even when an obstacle is embedded.

Fig. 11. Full wave simulation illustrating the wavefront shaping effect: (a) normalized electric field distribution (E_z) for PhC-TM05; (b) control simulation with the PhC-TM05 removed; (c) normalized magnetic field distribution (H_z) for PhC-TE06; (d) control simulation with the PhC-TE06 removed.

Fig. 12. Full wave simulation demonstrating that waves can turn a bent waveguide with embedded obstacles: (a) normalized electric field distribution (E_z) for PhC-TM05; (b) control simulation with the PhC-TM05 removed; (c) normalized magnetic field distribution (H_z) for PhC-TE06; (d) control simulation with the PhC-TE06 removed.

6. Topology optimization for extended Dirac-like problems

The developed topology optimization can be equally extended for other Dirac-like problems. For example, PhCs with one Dirac-like cone at ω and one monopolar band at 2ω at the Γ point can be exploited for the phase-matched second harmonic generation [12]. In addition, by judiciously introducing nonhermiticity to give rise to exceptional points (EPs), this structure can be exploited to enhance the efficiency of nonlinear frequency conversion [11]. Here, this paper demonstrates two optimized PhCs exhibiting this characteristic for TM modes, as given in Fig. 13. To obtain the optimized structures, the maximum of $1/L_1$ and $1/L_2$ at ω and $1/L_3$ at 2ω is minimized, which is equivalent to maximize the minimum of L_1 and L_2 at ω and L_1 at 2ω . As can be observed in the band structures, at the desired frequencies $\omega a/2\pi c = 0.5$ and 0.6 , two D modes and one M mode (red lines) are degenerated at the Γ point forming the Dirac-like cone, while one higher order M mode (blue line) is located at the frequency of 2ω .

Fig. 13. Optimized topologies for PhCs with one Dirac-like cone at ω and one higher-order M mode at 2ω , and their band structures: (a,d) optimized 3×3 primitive unit cells for $\omega a/2\pi c = 0.5$ and 0.6 , respectively; (b,e) corresponding band structures, the inserts denote two D modes (D1 and D2) and one M mode (M1) forming the Dirac-like cone at ω and one higher-order M mode (M2) at 2ω ; (c,f) close-up of three-dimensional dispersion surfaces near the Dirac-like cone (denoted as a dashed box in the band structure).

The third-order Dirac-like cone, in which M, D, Q modes are simultaneously degenerated at the Γ point, can be exploited to create third-order EP by introducing non-hermiticity, leading to strong enhancement of the spontaneous emission of emitters located at the PhC [9]. To design a third-order Dirac-like cone, the maximum of $\{1/L_1, 1/L_2, 1/L_3\}$ is minimized, which is equivalent to maximize the minimum of $\{L_1, L_2, L_3\}$. The lattice is enforced with C_{2v} symmetry, as it must break the C_{4v} symmetry of the lattice to obtain the third-order Dirac-like cone [9]. The corresponding irreducible Brillouin zone is demonstrated in the insert of Fig. 14(b). This paper aims to design a third-order Dirac-like cone for TM modes and consider both low index material, $\epsilon_2 = 3.3$, and high index material, $\epsilon_2 = 9$, in air, $\epsilon_1 = 1$. Figure 14 demonstrates the optimized PhCs and their band structures. The Dirac frequencies are $\omega a/2\pi c = 0.8$ and 0.5 for low index PhC and high index PhC, respectively. These third-order Dirac-like cones are formed by the degeneracy of M, D and Q modes belonging to three different representations; the A_1 , A_2 and B_1 representations of the C_{2v} group. As shown in Figs. 14 (c) and (f), in the vicinity of the third-order Dirac-like cone, the band structures exhibit conical Dirac dispersion (blue and green) accompanied by a flat band (red). Compared to the PhCs with third-order Dirac-like cones in reference [9], both the optimized low index and high index PhCs have regular and relatively smooth features, making them accessible to be fabricated by standard lithography or laser-writing method.

Fig. 14. Optimized PhCs with third-order Dirac-like cones and their band structures: (a,d) optimized 3×3 primitive unit cells for low index material and high index material, respectively; (b,e) corresponding band structures, the inserts denote that the third-order

Dirac-like cones are formed by the degeneracy of M, D and Q modes; (c,f) close-up of three-dimensional dispersion surfaces near the third-order Dirac-like cone (denoted as a dash box in the band structure).

7. Conclusion

This paper systematically investigates the design of Dirac-like cones in PhCs using the two-stage topology optimization, MMA-ETO. By maximizing the minimum of a collection of LDOSSs corresponding to different judiciously selected sources, Dirac-like cones formed by the degeneracy of doubly degenerate modes (D modes) and a single mode (M or Q mode) at different desired frequencies are successfully obtained for both TM mode and TE mode. Based on the optimized PhCs, exotic wave manipulation properties associated with Dirac-like cones, such as cloaking, wavefront shaping and tunneling through bent channels, are exhibited through full wave simulation. The proposed method is also effective for extended Dirac-like problems, such as designing PhCs with a Dirac-like cone at frequency ω and a high-order M mode at frequency 2ω and PhCs with third-order Dirac-like cones, which have potential applications in nonlinear optics. All optimized topologies are first reported and have regular and smooth features, making them be readily fabricated. Future work will consider the design of exceptional points based on the optimized PhCs by introducing non-hermiticity, the experimental realization of these designs and the optimization of Dirac-like cones in three-dimensional PhCs.

Acknowledgements

The authors wish to acknowledge the financial support from the Australian Research Council (FT130101094) and the China Scholarship Council.

References

- [1] X. Zhang, Observing Zitterbewegung for photons near the Dirac point of a two-dimensional photonic crystal, *Physical Review Letters* 100(11) (2008) 2339-2340.
- [2] X. Huang, Y. Lai, Z.H. Hang, H. Zheng, C.T. Chan, Dirac cones induced by accidental degeneracy in photonic crystals and zero-refractive-index materials, *Nature Materials* 10(8) (2011) 582-586.
- [3] Y. Li, S. Kita, P. Muñoz, O. Reshef, D.I. Vulis, M. Yin, M. Lončar, E. Mazur, On-chip zero-index metamaterials, *Nature Photonics* 9(11) (2015) 738-742.
- [4] I. Liberal, N. Engheta, Near-zero refractive index photonics, *Nature Photonics* 11(3) (2017) 149-158.
- [5] X. Niu, X. Hu, S. Chu, Q. Gong, Epsilon-Near-Zero Photonics: A New Platform for Integrated Devices, *Advanced Optical Materials* 6(10) (2018) 1701292.
- [6] S. Raghu, F.D.M. Haldane, Analogs of quantum-Hall-effect edge states in photonic crystals, *Physical Review A* 78(3) (2006) 033834.
- [7] R. Interets, Photonic topological insulators, *Nature Materials* 12(3) (2013) 233-239.
- [8] B. Zhen, C.W. Hsu, Y. Igarashi, L. Lu, I. Kaminer, A. Pick, S.L. Chua, J.D. Joannopoulos, M. Soljačić, Spawning rings of exceptional points out of Dirac cones, *Nature* 525(7569) (2015) 354-358.
- [9] Z. Lin, A. Pick, M. Lončar, A.W. Rodriguez, Enhanced Spontaneous Emission at Third-Order Dirac Exceptional Points in Inverse-Designed Photonic Crystals, *Physical Review Letters* 117(10) (2016) 107402.

- [10] J. Mei, Y. Wu, C.T. Chan, Z.Q. Zhang, First-principles study of Dirac and Dirac-like cones in phononic and photonic crystals, *Physical Review B* 86(3) (2012) 035141.
- [11] A. Pick, Z. Lin, W. Jin, A.W. Rodriguez, Enhanced nonlinear frequency conversion and Purcell enhancement at exceptional points, *Physical Review B* 96(22) (2017) 224303.
- [12] N. Mattiucci, M.J. Bloemer, G. D'Aguanno, Phase-matched second harmonic generation at the Dirac point of a 2-D photonic crystal, *Optics Express* 22(6) (2014) 6381-6390.
- [13] N. Mattiucci, M.J. Bloemer, G. D'Aguanno, All-optical bistability and switching near the Dirac point of a 2-D photonic crystal, *Optics Express* 21(10) (2013) 11862.
- [14] C. Xu, Y. Lai, Configurable Dirac-like conical dispersions in complex photonic crystals, *Physical Review B* 95(4) (2017) 045124.
- [15] M.P. Bendsøe, Optimal shape design as a material distribution problem, *Structural Optimization* 1(4) (1989) 193-202.
- [16] M.P. Bendsøe, O. Sigmund, *Topology optimization: Theory, Methods, and Applications*, Springer-Verlag, Berlin, 2003.
- [17] M.Y. Wang, X. Wang, D. Guo, A level set method for structural topology optimization, *Computer Methods in Applied Mechanics and Engineering* 192(1) (2003) 227-246.
- [18] X. Huang, Y. Xie, *Evolutionary topology optimization of continuum structures: methods and applications*, John Wiley & Sons, 2010.
- [19] K. Svanberg, *A Class of Globally Convergent Optimization Methods Based on Conservative Convex Separable Approximations*, Society for Industrial and Applied Mathematics, 2002.
- [20] J.S. Jensen, O. Sigmund, Topology optimization for nano□photronics, *Laser & Photonics Reviews* 5(2) (2011) 308-321.
- [21] X. Liang, S.G. Johnson, Formulation for scalable optimization of microcavities via the frequency-averaged local density of states, *Optics Express* 21(25) (2013) 30812-30841.
- [22] A.Y. Piggott, J. Lu, K.G. Lagoudakis, J. Petykiewicz, T.M. Babinec, J. Vučković, Inverse design and demonstration of a compact and broadband on-chip wavelength demultiplexer, *Nature Photonics* 9(6) (2015) 374-377.
- [23] L.H. Frandsen, Y. Elesin, L.F. Frellsen, M. Mitrovic, Y. Ding, O. Sigmund, K. Yvind, Topology optimized mode conversion in a photonic crystal waveguide fabricated in silicon-on-insulator material, *Optics Express* 22(7) (2014) 8525-8532.
- [24] B. Shen, P. Wang, R. Polson, R. Menon, An integrated-nanophotonics polarization beamsplitter with $2.4 \times 2.4 \mu\text{m}^2$ footprint, *Nature Photonics* 9(6) (2015) 378-382.
- [25] Z. Lin, X. Liang, M. Lončar, S.G. Johnson, A.W. Rodriguez, Cavity-enhanced second-harmonic generation via nonlinear-overlap optimization, *Optica* 3(3) (2016) 233-238.
- [26] F. Meng, X. Huang, B. Jia, Bi-directional evolutionary optimization for photonic band gap structures, *Journal of Computational Physics* 302 (2015) 393-404.
- [27] F. Meng, Y. Li, S. Li, H. Lin, B. Jia, X. Huang, Achieving large band gaps in 2D symmetric and asymmetric photonic crystals, *Journal of Lightwave Technology* 35(9) (2017) 1670-1676.
- [28] F. Meng, S. Li, Y. Li, B. Jia, X. Huang, Microstructural design for 2D photonic crystals with large polarization-independent band gaps, *Materials Letters* 207 (2017) 176-178.
- [29] J. Vester-Petersen, R.E. Christiansen, B. Julsgaard, P. Balling, O. Sigmund, S.P. Madsen, Topology optimized gold nanostrips for enhanced near-infrared photon upconversion, *Applied Physics Letters* 111(13) (2017) 133102.
- [30] J.S. Jensen, O. Sigmund, Systematic design of photonic crystal structures using topology optimization: Low-loss waveguide bends, *Applied Physics Letters* 84(12) (2004) 2022-2024.
- [31] O. Sigmund, K. Hougaard, Geometric properties of optimal photonic crystals, *Physical Review Letters* 100(15) (2008) 153904.
- [32] F. Wang, J.S. Jensen, O. Sigmund, Robust topology optimization of photonic crystal

- waveguides with tailored dispersion properties, Journal of the Optical Society of America B 28(3) (2011) 387-397.
- [33] S. Zhou, W. Li, Y. Chen, G. Sun, Q. Li, Topology optimization for negative permeability metamaterials using level-set algorithm, Acta Materialia 59(7) (2011) 2624-2636.
- [34] G.L. Yi, B.D. Youn, A comprehensive survey on topology optimization of phononic crystals, Structural and Multidisciplinary Optimization 54(5) (2016) 1315-1344.
- [35] S. Molesky, Z. Lin, A.Y. Piggott, W. Jin, J. Vuckovic, A.W. Rodriguez, Outlook for inverse design in nanophotonics, arXiv preprint arXiv:1801.06715v1 (2018).
- [36] Z. Lin, L. Christakis, Y. Li, E. Mazur, A.W. Rodriguez, M. Lončar, Topology-optimized Dual-Polarization Dirac Cones, Physical Review B 97(8) (2018) 081408(R).
- [37] J. Nocedal, S.J. Wright, Numerical Optimization, Springer1999.
- [38] J.D. Joannopoulos, S.G. Johnson, J.N. Winn, R.D. Meade, Photonic crystals: molding the flow of light, Princeton university press, 2011.
- [39] D.R. Smith, D.C. Vier, T. Koschny, C.M. Soukoulis, Electromagnetic parameter retrieval from inhomogeneous metamaterials, Physical Review E 71(3) (2005) 036617.

Figure Captions:

Fig. 1. Schematic diagram for the position of the source to obtain the desired mode: (a) \mathbf{J}_1 for M mode; (b) \mathbf{J}_2 for D mode; (c) \mathbf{J}_3 for Q mode.

Fig. 2. Iteration history of $\min(L_1, L_2)$, Dirac error and topology of primitive unit cell.

Fig. 3. Optimized PhCs and their band diagrams for TM modes: (a,d) optimized 3×3 primitive unit cells (light blue-dielectric material, white-air, hereinafter the same) for $\omega a/2\pi c = 0.5$ and 0.6 , respectively; (b,e) corresponding band structures, the inserts denote that the Dirac-like cones are formed by the degeneracy of two D modes and one M mode; (c,f) zooms in of three-dimensional dispersion surfaces near the Dirac-like cones (denoted as dash box in the band structure), k_x and k_y denote the Bloch wave vector along x and y direction, respectively.

Fig. 4. Optimized PhCs and their band diagrams for TE modes: (a,d) optimized 3×3 primitive unit cells (light blue - dielectric material, white - air, hereinafter the same) for $\omega a/2\pi c = 0.6$ and 0.7 , respectively; (b,e) corresponding band structures, the inserts denote that the Dirac-like cone is formed by the degeneracy of two D modes and one single mode (M or Q); (c,f) close-up of three-dimensional dispersion surfaces close to the Dirac-like cones (denoted as a dash box in the band structure).

Fig. 5. Mesh, smooth boundary, density of grid points x_j , and volume fraction of an element x_e are used in ETO.

Fig. 6. Iteration history of $\min(L_1, L_2)$, Dirac error and topology of primitive unit cell resulting from ETO.

Fig. 7. Optimized PhCs for Dirac-like cones of TM modes at different frequencies by ETO, their band structures and close-ups in of three-dimensional dispersion surfaces near the Dirac-like cones: (a) $\omega a/2\pi c = 0.50$; (b) $\omega a/2\pi c = 0.55$; (c) $\omega a/2\pi c = 0.60$.

Fig. 8. Optimized PhCs for Dirac-like cones of TE modes at different frequencies by ETO, their band structures and close-ups of three-dimensional dispersion surfaces near the Dirac-like cones: (a) $\omega a/2\pi c = 0.60$; (b) $\omega a/2\pi c = 0.65$; (c) $\omega a/2\pi c = 0.70$.

Fig. 9. Effective permittivity (ϵ_{eff}) and permeability (μ_{eff}) for PhC-TM05 and PhC-TE06.

Fig. 10. Full wave simulation illustrating the cloaking effect: (a) normalized electric field distribution (E_z) for PhC-TM05; (b) control simulation with the PhC-TM05 removed; (c) normalized magnetic field distribution (H_z) for PhC-TE06; (d) control simulation with the PhC-TE06 removed.

Fig. 11. Full wave simulation illustrating the wavefront shaping effect: (a) normalized electric field distribution (E_z) for PhC-TM05; (b) control simulation with the PhC-TM05 removed; (c) normalized magnetic field distribution (H_z) for PhC-TE06; (d) control simulation with the PhC-TE06 removed.

Fig. 12. Full wave simulation demonstrating that waves can turn a bent waveguide with embedded obstacles: (a) normalized electric field distribution (E_z) for PhC-TM05; (b) control simulation with the PhC-TM05 removed; (c) normalized magnetic field distribution (H_z) for PhC-TE06; (d) control simulation with the PhC-TE06 removed.

Fig. 13. Optimized topologies for PhCs with one Dirac-like cone at ω and one higher-order

M mode at 2ω , and their band structures: (a,d) optimized 3×3 primitive unit cells for $\omega a/2\pi c = 0.5$ and 0.6, respectively; (b,e) corresponding band structures, the inserts denote two D modes (D1 and D2) and one M mode (M1) forming the Dirac-like cone at ω and one higher-order M mode (M2) at 2ω ; (c,f) close-up of three-dimensional dispersion surfaces near the Dirac-like cone (denoted as a dash box in the band structure).

Fig. 14. Optimized PhCs with third-order Dirac-like cones and their band structures: (a,d) optimized 3×3 primitive unit cells for low index material and high index material, respectively; (b,e) corresponding band structures, the inserts denote that the third-order Dirac-like cones are formed by the degeneracy of M, D and Q modes; (c,f) close-up of three-dimensional dispersion surfaces near the third-order Dirac-like cone (denoted as a dash box in the band structure).

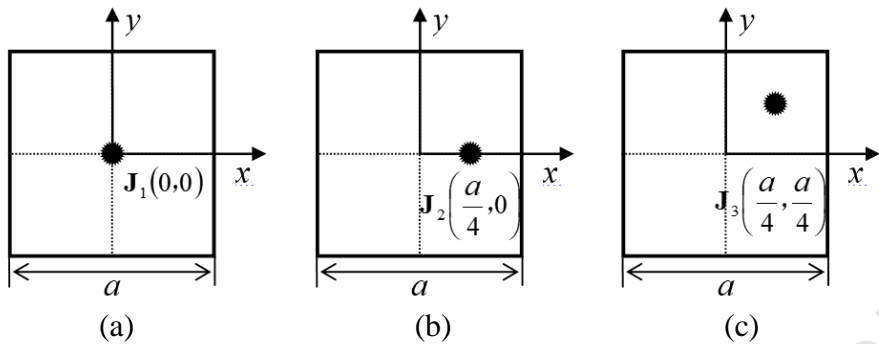


Fig. 1. Schematic diagram for the position of the source to obtain the desired mode: (a) \mathbf{J}_1 for M mode; (b) \mathbf{J}_2 for D mode; (c) \mathbf{J}_3 for Q mode.

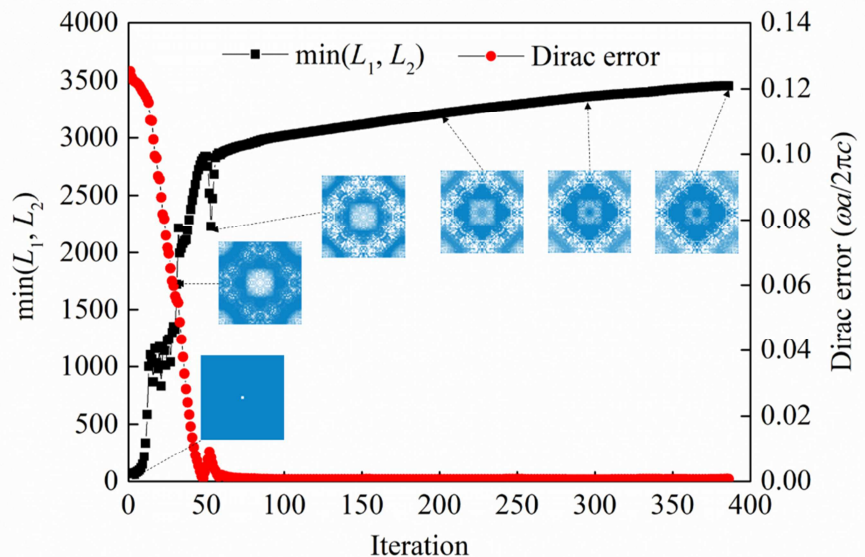


Fig. 2. Iteration history of $\min(L_1, L_2)$, Dirac error and topology of primitive unit cell.

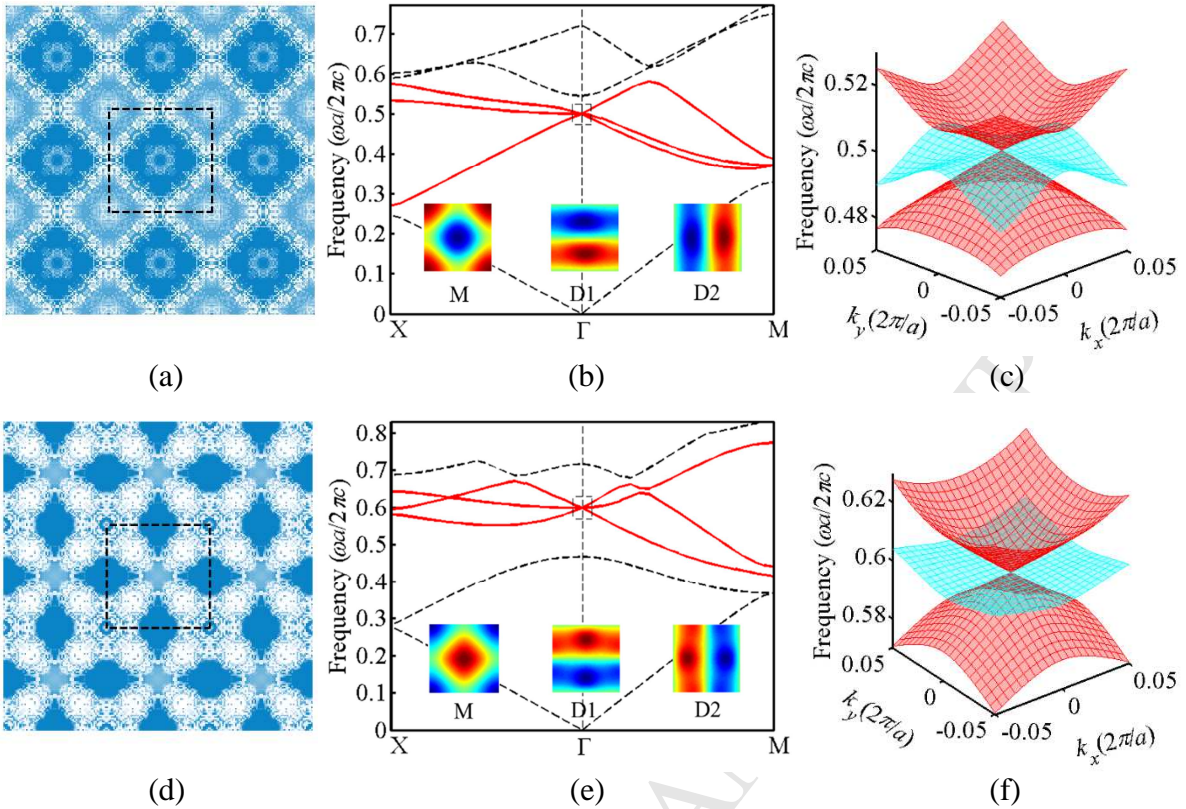


Fig. 3. Optimized PhCs and their band diagrams for TM modes: (a,d) optimized 3×3 primitive unit cells (light blue-dielectric material, white-air, hereinafter the same) for $\alpha a/2\pi c = 0.5$ and 0.6 , respectively; (b,e) corresponding band structures, the inserts denote that the Dirac-like cones are formed by the degeneracy of two D modes and one M mode; (c,f) zooms in of three-dimensional dispersion surfaces near the Dirac-like cones (denoted as dash box in the band structure). k_x and k_y denote the Bloch wave vector along the direction x and y , respectively.

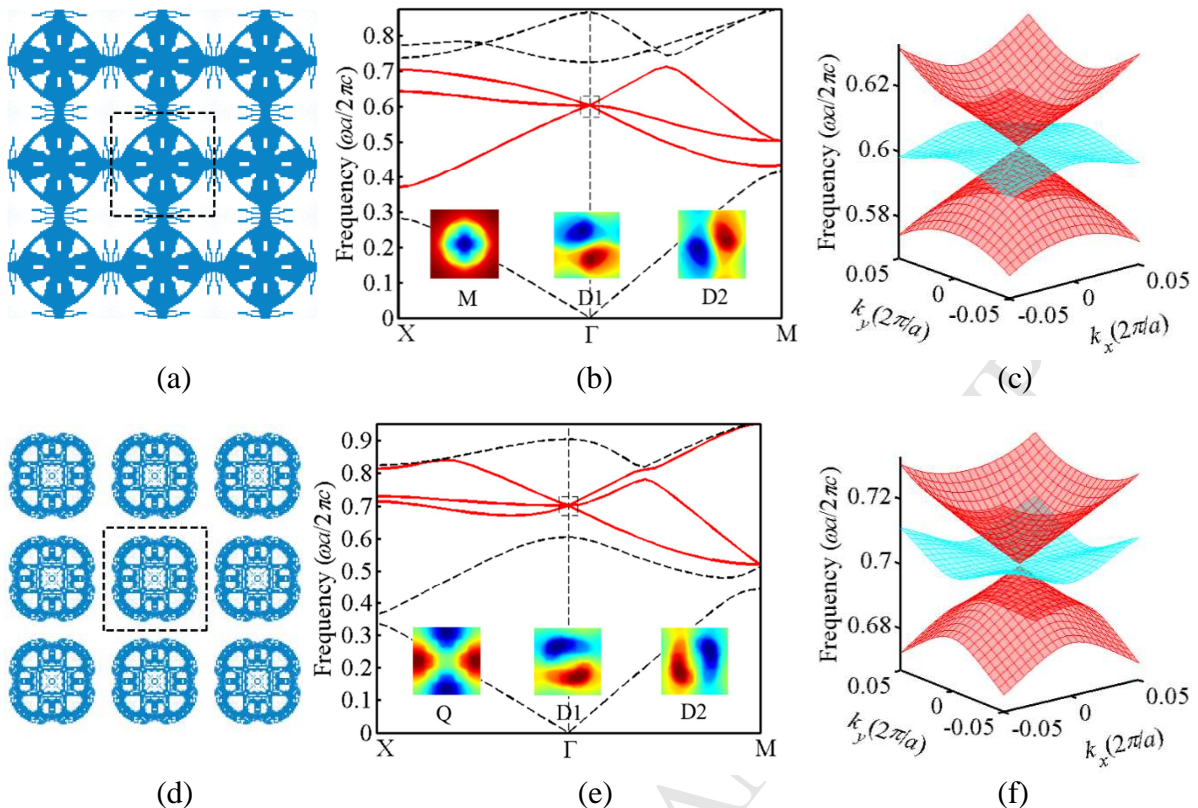


Fig. 4. Optimized PhCs and their band diagrams for TE modes: (a,d) optimized 3×3 primitive unit cells (light blue - dielectric material, white - air, hereinafter the same) for $\omega a/2\pi c = 0.6$ and 0.7, respectively; (b,e) corresponding band structures, the inserts denote that the Dirac-like cone is formed by the degeneracy of two D modes and one single mode (M or Q); (c,f) close-up of three-dimensional dispersion surfaces close to the Dirac-like cones (denoted as a dash box in the band structure).

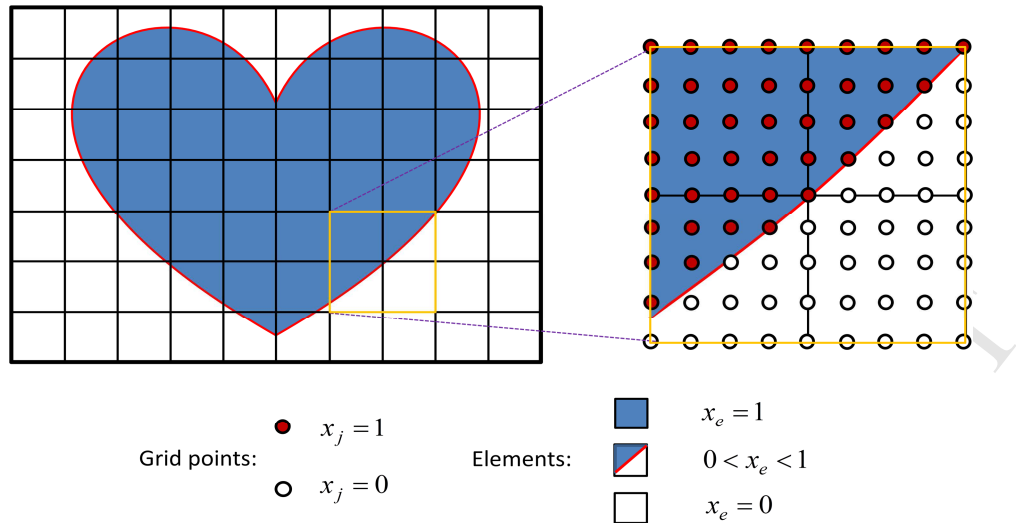


Fig. 5. Mesh, smooth boundary, density of grid points x_j , and volume fraction of an element x_e are used in ETO.

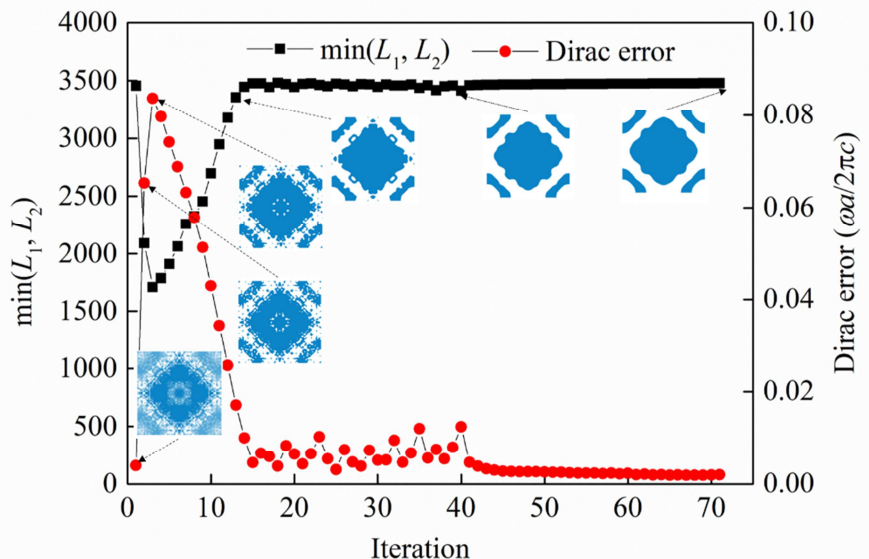


Fig. 6. Iteration history of $\min(L_1, L_2)$, Dirac error and topology of primitive unit cell resulting from ETO.

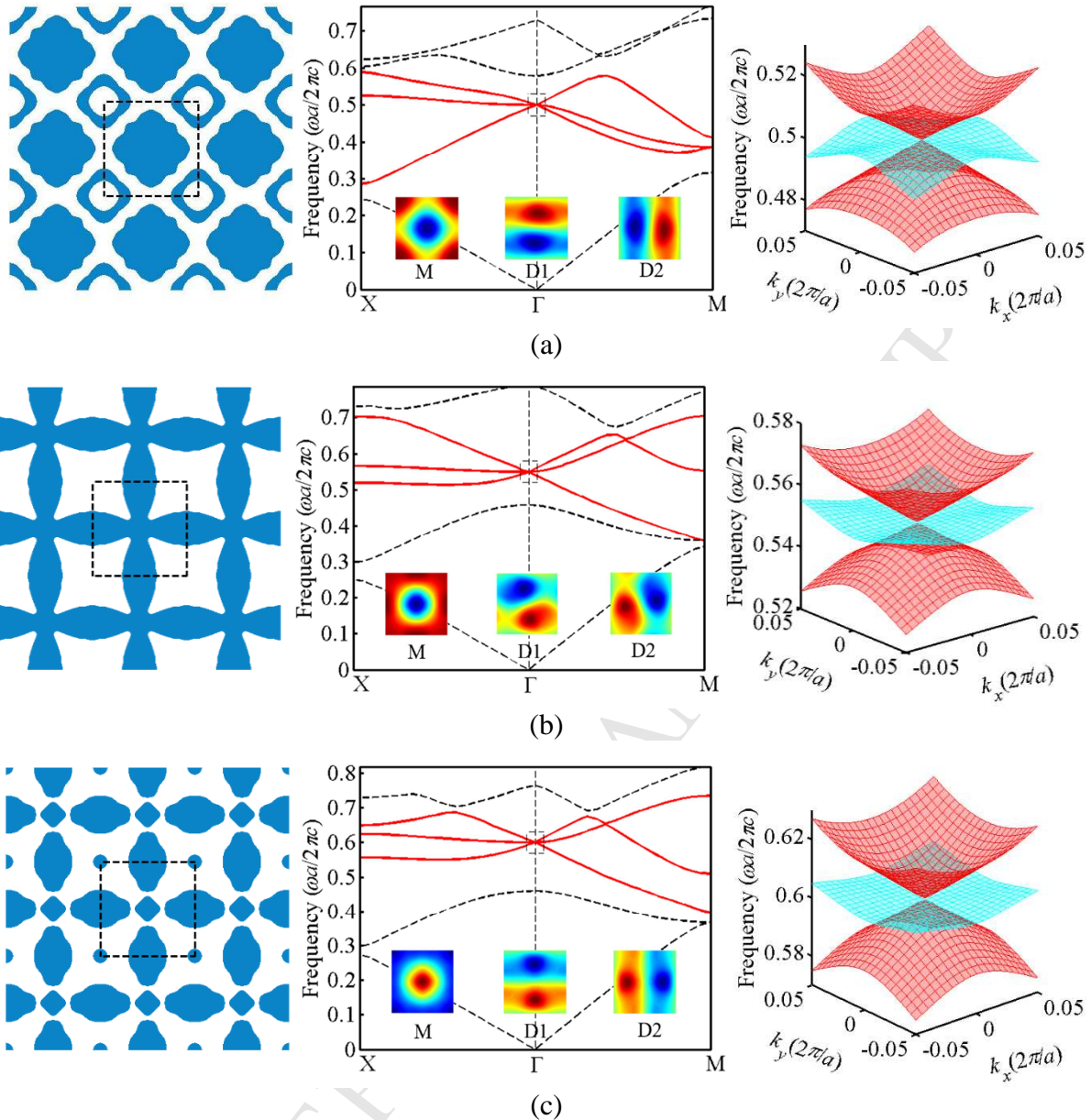


Fig. 7. Optimized PhCs for Dirac-like cones of TM modes at different frequencies by ETO, their band structures and close-ups in of three-dimensional dispersion surfaces near the Dirac-like cones: (a) $\omega a/2\pi c = 0.50$; (b) $\omega a/2\pi c = 0.55$; (c) $\omega a/2\pi c = 0.60$.

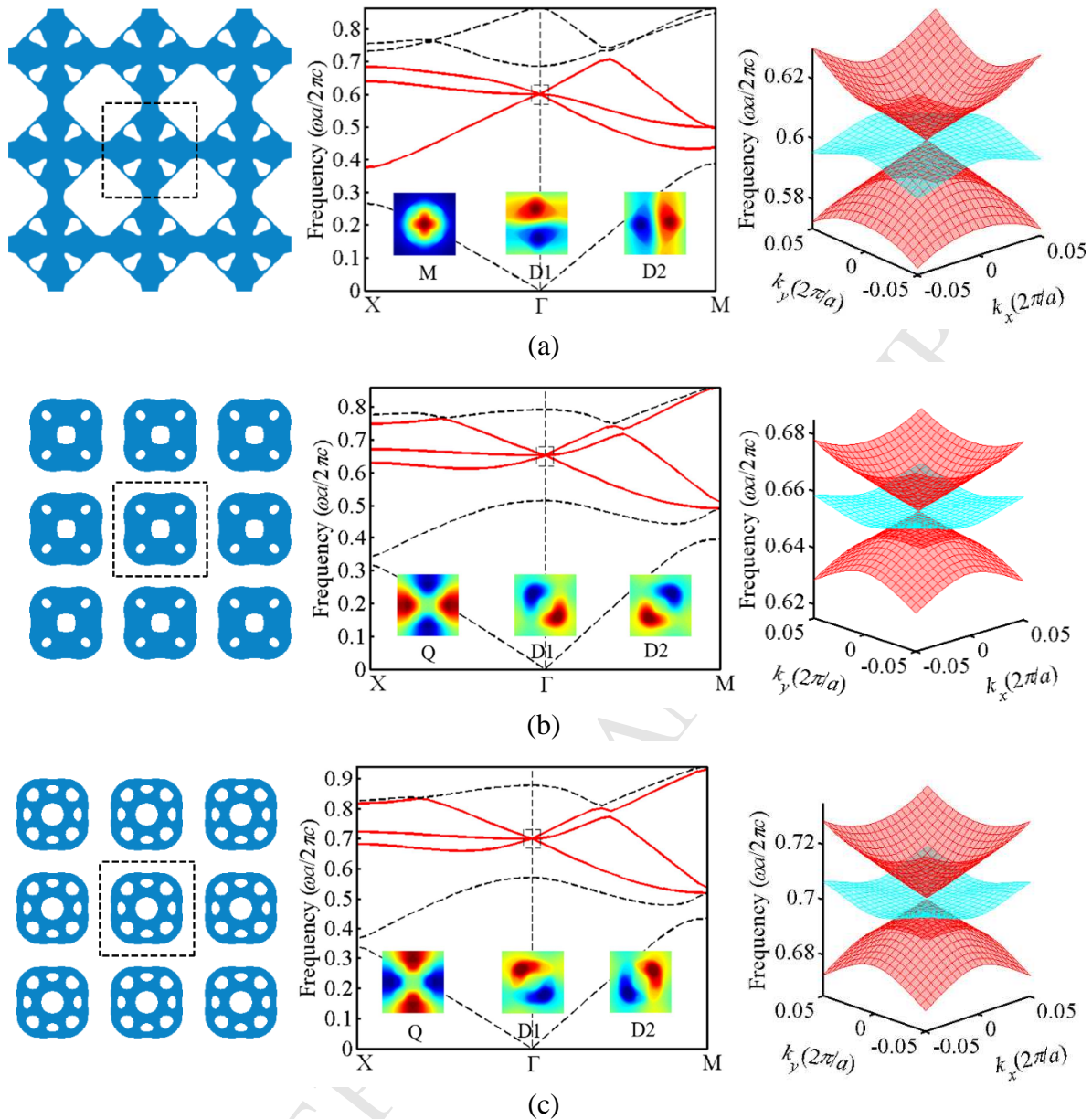


Fig. 8. Optimized PhCs for Dirac-like cones of TE modes at different frequencies by ETO, their band structures and close-ups of three-dimensional dispersion surfaces near the Dirac-like cones: (a) $\omega a/2\pi c = 0.60$; (b) $\omega a/2\pi c = 0.65$; (c) $\omega a/2\pi c = 0.70$.

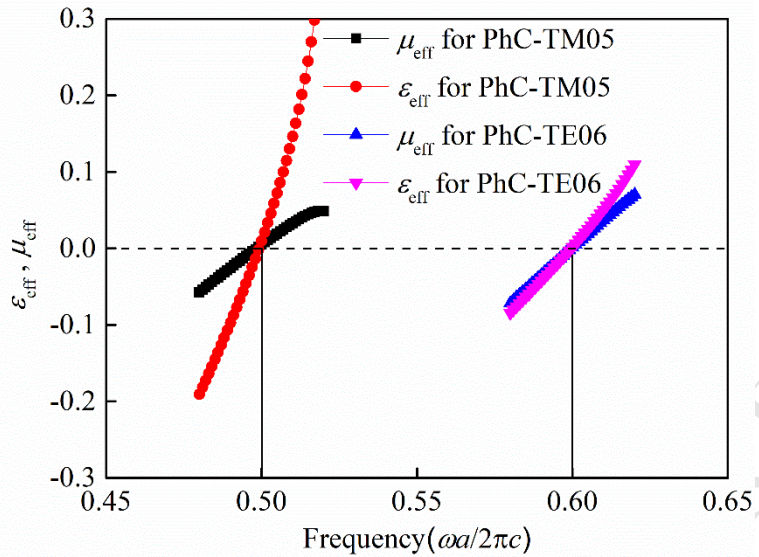


Fig. 9. Effective permittivity (ϵ_{eff}) and permeability (μ_{eff}) for PhC-TM05 and PhC-TE06

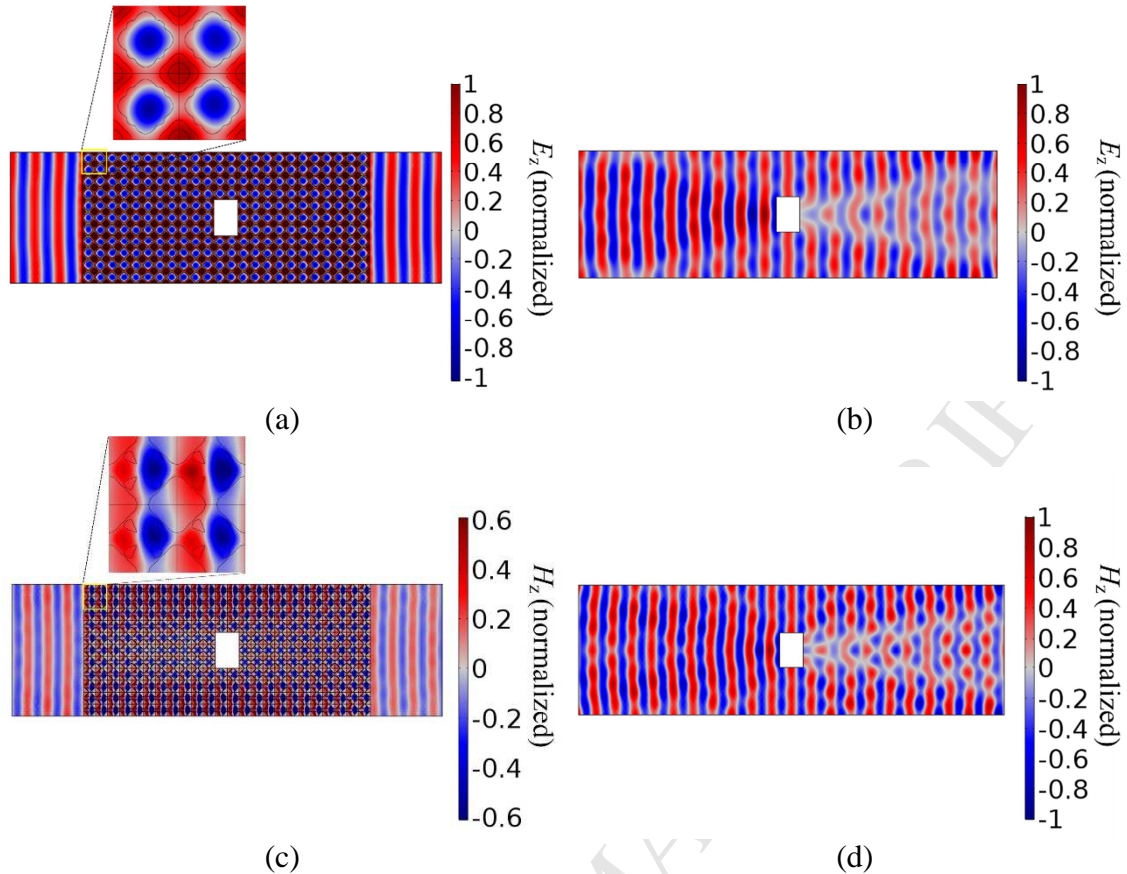


Fig. 10. Full wave simulation illustrating the cloaking effect: (a) normalized electric field distribution (E_z) for PhC-TM05; (b) control simulation with the PhC-TM05 removed; (c) normalized magnetic field distribution (H_z) for PhC-TE06; (d) control simulation with the PhC-TE06 removed.

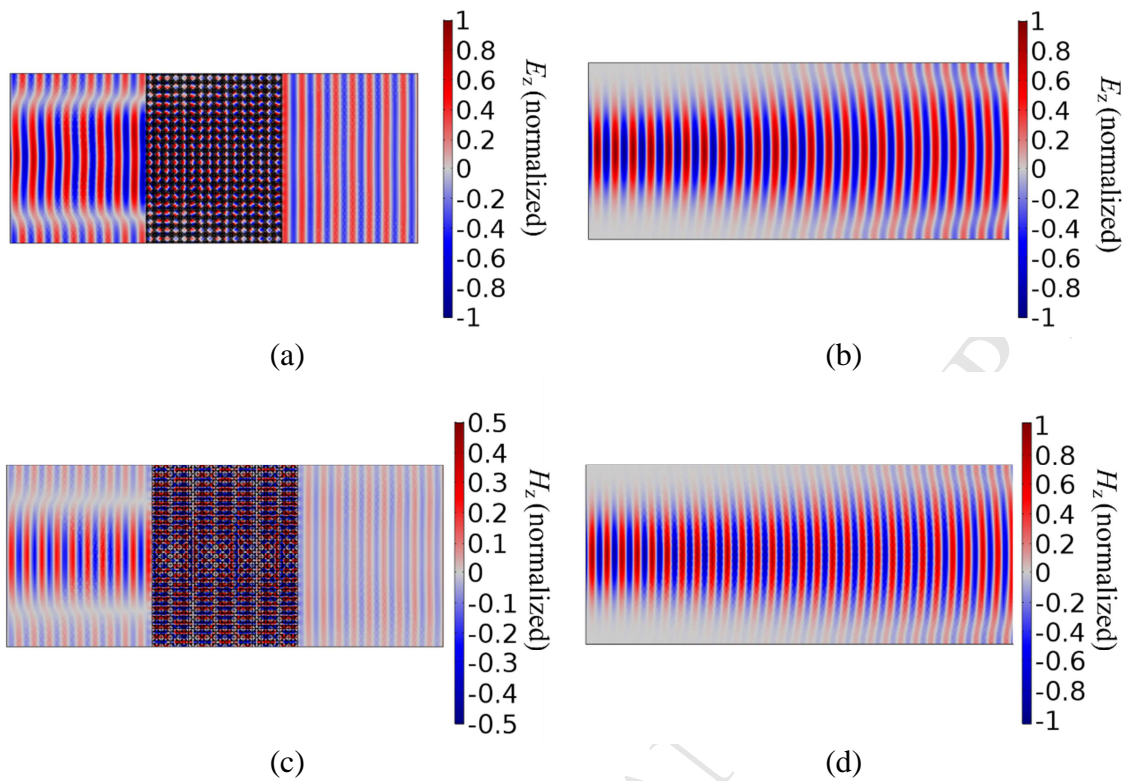


Fig. 11. Full wave simulation illustrating the wavefront shaping effect: (a) normalized electric field distribution (E_z) for PhC-TM05; (b) control simulation with the PhC-TM05 removed; (c) normalized magnetic field distribution (H_z) for PhC-TE06; (d) control simulation with the PhC-TE06 removed.

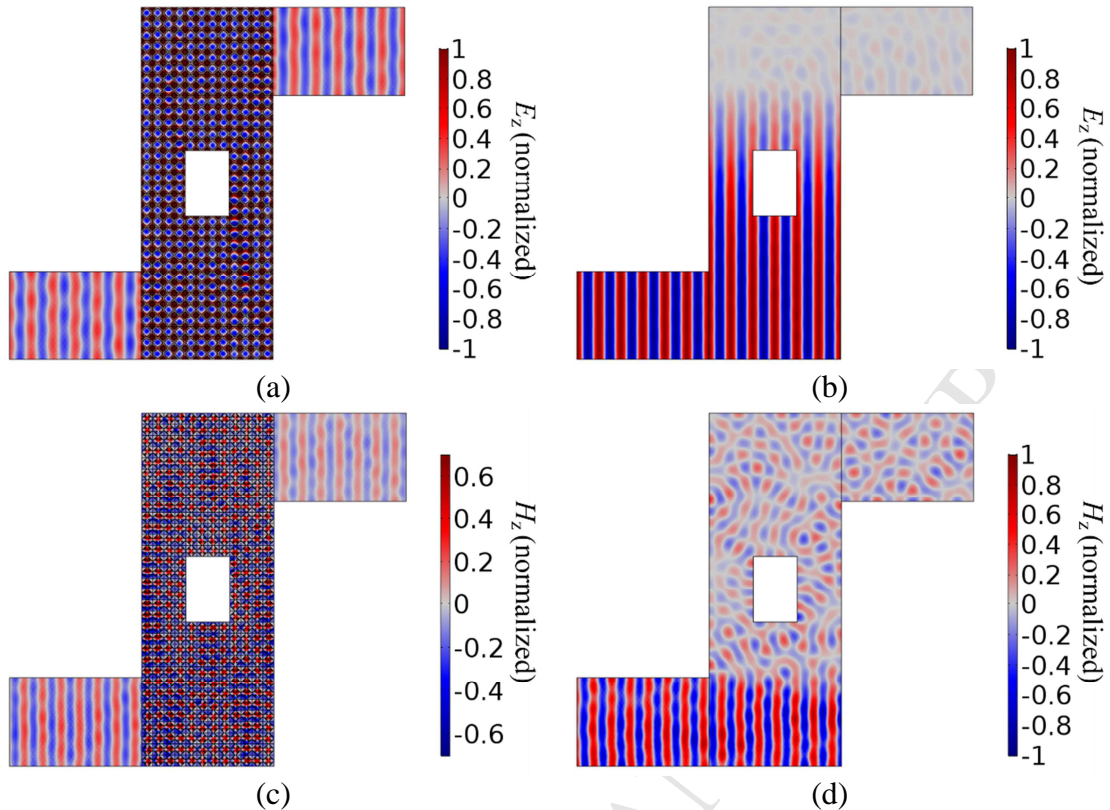


Fig. 12. Full wave simulation demonstrating that waves can turn a bent waveguide with embedded obstacles: (a) normalized electric field distribution (E_z) for PhC-TM05; (b) control simulation with the PhC-TM05 removed; (c) normalized magnetic field distribution (H_z) for PhC-TE06; (d) control simulation with the PhC-TE06 removed.

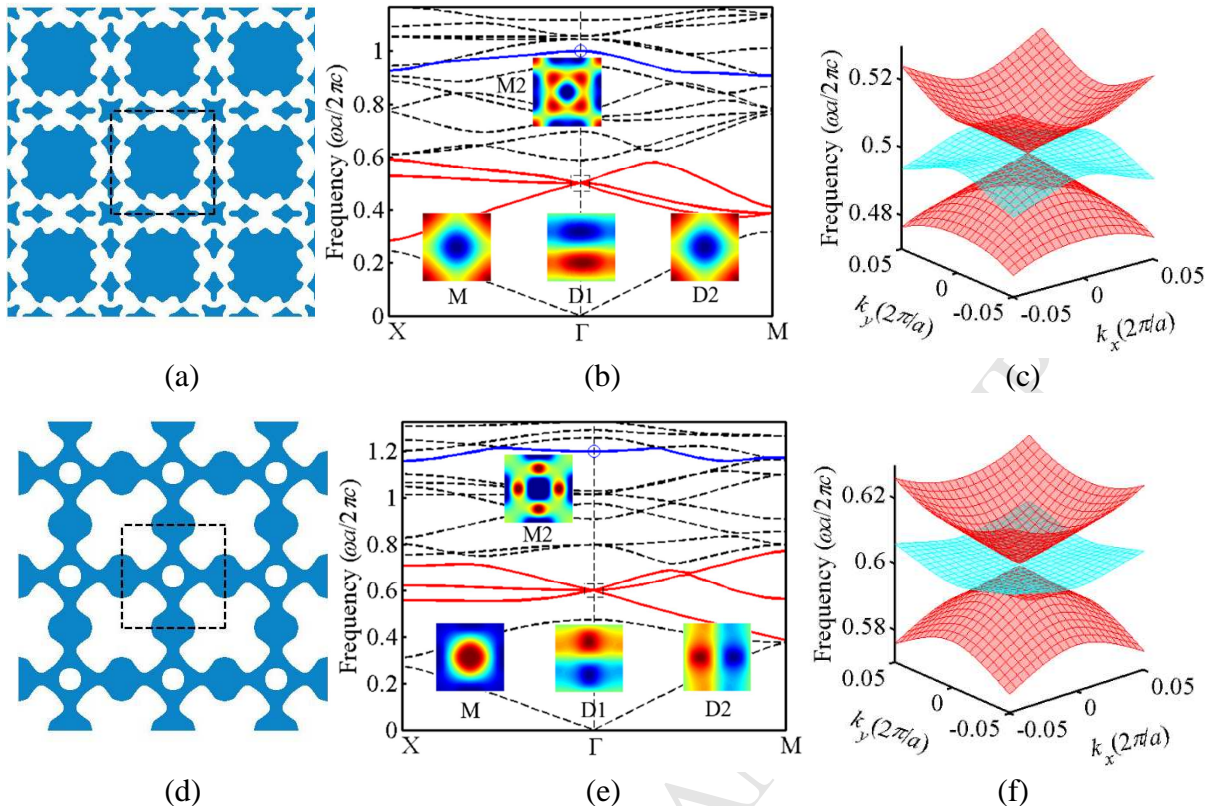


Fig. 13. Optimized topologies for PhCs with one Dirac-like cone at ω and one higher-order M mode at 2ω , and their band structures: (a,d) optimized 3×3 primitive unit cells for $\omega a/2\pi c = 0.5$ and 0.6 , respectively; (b,e) corresponding band structures, the inserts denote two D modes (D1 and D2) and one M mode (M1) forming the Dirac-like cone at ω and one higher-order M mode (M2) at 2ω ; (c,f) close-up of three-dimensional dispersion surfaces near the Dirac-like cone (denoted as a dash box in the band structure).

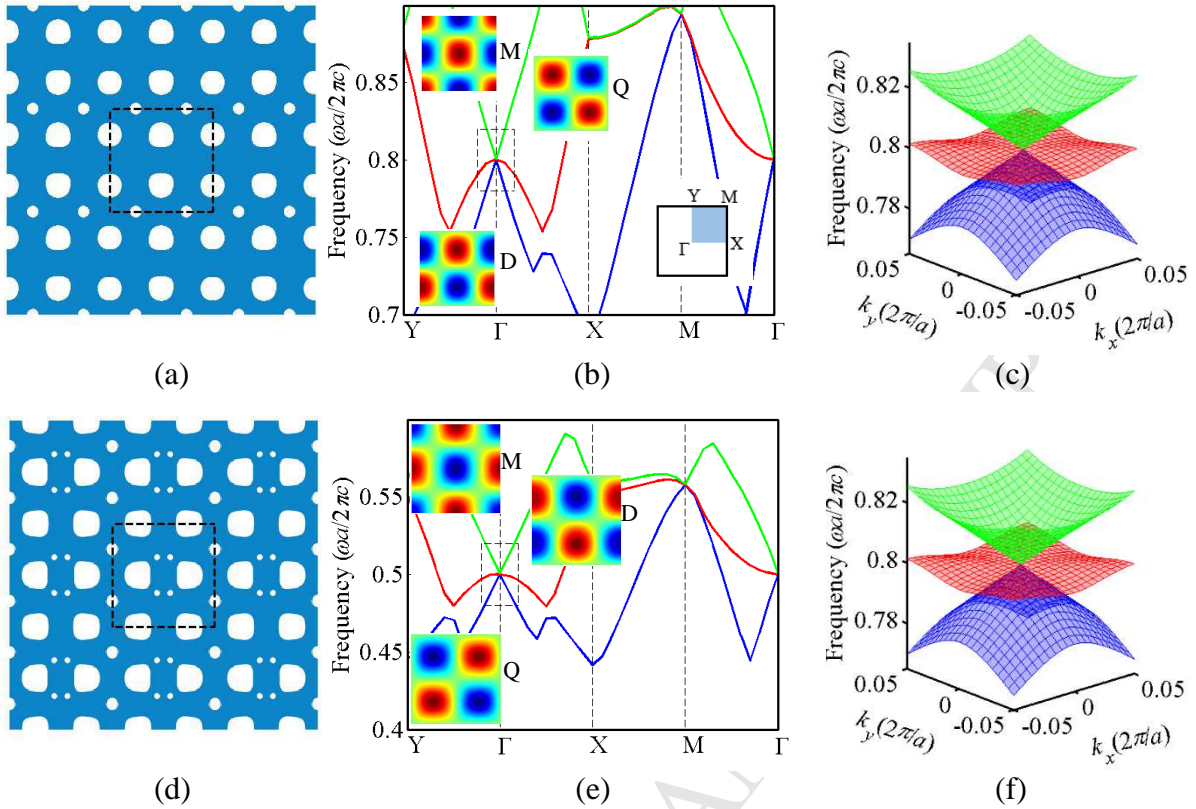


Fig. 14. Optimized PhCs with third-order Dirac-like cones and their band structures: (a,d) optimized 3×3 primitive unit cells for low index material and high index material, respectively; (b,e) corresponding band structures, the inserts denote that the third-order Dirac-like cones are formed by the degeneracy of M, D and Q modes; (c,f) close-up of three-dimensional dispersion surfaces near the third-order Dirac-like cone (denoted as a dash box in the band structure).